Size-Dependent Multi-Electron Donation in Metal-Complex Quantum Dots Hybrid Catalyst for Photocatalytic Carbon Dioxide Reduction

Zhao, Qian; Abdellah, Mohamed; Cao, Yuehan; Meng, Jie; Zou, Xianshao; Enemark-Rasmussen, Kasper; Lin, Weihua; Li, Yi; Chen, Yijiang; Duan, Hengli

Total number of authors:
17

Published in:
Advanced Functional Materials

Link to article, DOI:
10.1002/adfm.202315734

Publication date:
2024

Document Version
Publisher's PDF, also known as Version of record

ADVANCED FUNCTIONAL MATERIALS
www.afm-journal.de

Size-Dependent Multi-Electron Donation in Metal-Complex Quantum Dots Hybrid Catalyst for Photocatalytic Carbon Dioxide Reduction

Qian Zhao, Mohamed Abdellah, Yuehan Cao, Jie Meng, Xianshao Zou, Kasper Ene-mark-Rasmussen, Weihua Lin, Yi Li, Yijiang Chen, Hengli Duan, Qinying Pan, Ying Zhou, Tonu Pullerits, Hong Xu, Sophie E. Canton, Yuran Niu, and Kaibo Zheng**

The effective conversion of carbon dioxide (CO_2) into valuable chemical fuels relies significantly on the donation of multiple electrons. Its efficiency is closely linked to both the density and lifetime of excited charge carriers. In this study, a hybrid catalyst system comprising covalently bonded InP/ZnS quantum dots (QDs) and Re-complexes is showcased. The electronic band alignment between the QDs and the Re-complexes is revealed to dominate the multi-electron transfer process for photocatalytic conversion to methane (CH_4). Notably, the size of the QDs is found to be a determining parameter. Among the three QD sizes investigated, transient absorption spectroscopy studies unveil that rapid multi-electron transfer from the QDs to the Re-catalyst occurs in smaller QDs (2.3 nm) due to the substantial driving force. Consequently, the photocatalytic conversion of CO_2 to CH_4 is significantly enhanced with a turnover number of 6, corresponding to the overall apparent quantum yield of ≈1%. This research underscores the possibilities of engineering multi-electron transfer by manipulating the electronic band alignment within a catalytic system. This can serve as a guide for optimizing photocatalytic CO_2 reduction.

1. Introduction

Photocatalytic reduction for the conversion of CO_2 into value-added products, such as short-chain chemical fuels or even materials, is seen as a promising solution to address the challenges posed by the escalating energy shortage and resulting greenhouse gas emissions contributing to global warming.[1] Unlike the photocatalytic evolution of H_2, the reduction of CO_2 through a single-electron-mediated process is highly endo-thermic due to the stability of the C═O bond in the CO_2 molecule.[2,3] Conversely, the production facilitated by multiple electrons is generally more energetically favorable, yielding products with reduced redox overpotential. However, achieving multi-electron donation after excitation requires photocatalysts with long-lived excited states, stable one-electron-reduction (OER) intermediates, and robust bonds between the

Q. Zhao, J. Meng, X. Zou, K. Ene-mark-Rasmussen, S. E. Canton, K. Zheng
Department of Chemistry
Technical University of Denmark
Kongens Lyngby DK-2800, Denmark
E-mail: kzheng@kemi.dtu.dk

M. Abdellah
Department of Chemistry
College of Science
United Arab Emirates University
P.O. Box 17551, Al Ain United Arab Emirates

M. Abdellah, J. Meng, X. Zou, W. Lin, H. Duan, Q. Pan, T. Pullerits, Y. Niu, K. Zheng
Chemical Physics and NanoLund
Lund University
Box 124, Lund 22100, Sweden

The ORCID identification number(s) for the author(s) of this article can be found under https://doi.org/10.1002/adfm.202315734

DOI: 10.1002/adfm.202315734

M. Abdellah
Department of Chemistry
Qena Faculty of Science
South Valley University
Qena 83523, Egypt

Y. Cao, Y. Li, Y. Chen, Y. Zhou
National Key Laboratory of Oil and Gas Reservoir Geology and Exploitation
Southwest Petroleum University
Chengdu 610500, China
E-mail: yzhou@swpu.edu.cn

H. Duan, Y. Niu
MAX IV Laboratory
Lund University
P.O. Box 118, Lund 22100, Sweden

H. Xu
Institute of Nuclear and New Energy Technology
Tsinghua University
Beijing 100084, China

CO_2 molecule and catalytic sites.[4] This challenge is particularly pronounced for the evolution of multi-electron reduction products like CH_4 or methanol (CH_3OH) compared to 2-electron reduction products such as carbon monoxide and formic acid.[5,6] In fact, CO_2 photocatalytic reduction is widely accepted as a sequential multi-step process:

$$CO_2 \xrightarrow{e^-,h^+} * COOH \xrightarrow{e^-,h^+} * CO \xrightarrow{e^-,h^+} * CHO \xrightarrow{e^-,h^+} * CH_2O \xrightarrow{e^-,h^+} * CH_3O \xrightarrow{e^-,h^+} * CH_3OH \quad (1)$$

where the lowly reduced products (e.g., CO, CH_2O) are also intermediates for the generation of highly reduced products (e.g., CH_3OH, CH_4).[7] Therefore, seeking suitable catalysts with efficient multi-electron donation capability and achieving precise control of the charge generation and accumulation on the catalytic sites of the photocatalysts becomes the critical issue in determining the activity and product selectivity of the CO_2 photocatalytic reduction.

Transition metal complexes, especially Re(I) complexes, have been regarded as promising candidates to achieve multi-electron donations for CO_2 catalytic reduction since 1) their lowest triplet excited state lifetime is sufficiently long to ensure efficient photoinduced electron transfer to catalytic sites; 2) transition metals are easy to fix CO_2 by strong bond;[8,9] 3) their OER species are stable in solution with low overpotential facilitating the subsequent electron transfer to CO_2 adducts. However, most of the Re(I) complexes feature narrow absorption bands in the visible region,[10] and fast triple-triple annihilation (TTA) prohibits multi-electron accumulation on a single molecule.[6] According to recent reports, the absorption response of Re(I) complexes can be extended by attaching photosensitizers to form hybrid catalysts,[11–14] The fast annihilation can be solved by employing multi-Re(I) centers to enlarge the spatial distance of the excited electrons in the reservoir pools before they can be donated to CO_2 adducts.[15,16] Recently, we demonstrated a novel hybrid catalyst structure with InP/ZnS quantum dot (QDs) covalently attached with multiple Re-catalysts to tackle these two problems concurrently. Multiple catalyst attachments enabled the efficient injection of multiple photoexcited electrons from one QD since each electron resides at each surface catalyst with long lifetime. However, in order to achieve precise control of the charge generation and accumulation, as mentioned above, one direct strategy in hybrid catalysts is to modulate the charge transfer dynamics between photosensitizers and surface catalysts. This is usually achieved by the engineering of energy alignment as well as the electronic coupling between the electron donors (i.e., photosensitizers) and electron acceptors (i.e., catalysts).[17–19] In molecular catalysts, the energy alignment is adjusted by the molecular structures and assembly, while in inorganic catalysts, it is tailored by the catalyst composition and surface structures. However, these methods do not always offer the flexibility to fine-tune charge transfer rates due to constraints on available molecular structures and inorganic compositions. QDs, on the other hand, exhibit size-tunable optical band gaps, which can be perfect vehicles for fine-tuning the driving force for the charge transfer process.

This study explores the size dependence of the QDs on the photo-induced charge transfer dynamics and the catalytic performance of CO_2 photoreduction. Considering that the electronic structure of QDs is significantly influenced by size within a strong quantum confinement regime, we prepared three InP/ZnS-Re complex catalysts with different QD sizes for photocatalytic CO_2 reduction. The results reveal that only the QD-Re catalyst with the smallest size of InP/ZnS QDs achieved photoinduced multi-electron transfer processes, leading to CH_4 evolution. This phenomenon is attributed to a large driving force between the conduction band of QDs and Re(I) redox level, leading to efficient photo-generated multi-electron accumulation on the Re(I) center. Additionally, we observed that the photoinduced hole-trapping process is also limited by QD size, influencing the CO_2 conversion process. This work introduces a new strategy for controlling multi-electron transfer and provides a fundamental method for optimizing photocatalytic selectivity and efficiency for CO_2 reduction.

2. Results and Discussion

2.1. Structural Characterization

InP/ZnS colloidal quantum dot (InP/ZnS) with different sizes were obtained according to the previous literature protocol with slight modifications.[20] After 2-mercaptoethanol (ME) capped the InP/ZnS QDs (InP/ZnS-ME) were prepared via ligand exchange method, Re-photocatalyst was covalently linked to InP/ZnS QDs by simple esterification reaction between hydroxyl and phosphate group. Size control of InP/ZnS QDs was generally achieved by tuning the concentration ratio of $ZnCl_2$ and ZnI_2 precursors as well as the growth temperature of InP core. (For a detailed synthesis procedure, see supporting information). Here, quantum dot/complex hybrid photocatalysts with different sizes of QDs were synthesized and defined by Re-2.3 nm, Re-3.3 nm, and Re-3.8 nm according to their average sizes confirmed by TEM characterization (**Figure 1**d–e). We have measured the HR-TEM of the Re-2.3 nm (a), Re-3.3 nm (b), and Re-3.8 nm (c) (Figure S1, Supporting Information), where a clear size increase among the three samples can be observed. The insets of the figures show the clear atomic assembly of the lattice with lattice spacing, all calculated to be 0.34 nm, which matches the (111) plane of the InP zinc blend structure. Furthermore, X-ray diffraction (XRD) was also measured for Re-2.3 nm, Re-3.3 nm, and Re-3.8 nm samples, as well as neat InP/ZnS core-shell QDs (Figure S2, Supporting Information). The XRD patterns of all samples featured mainly the diffraction peaks of InP zinc blende, which are consistent with the TEM characterization with boardening of the peak due to the size reduction effect of the nanoparticle. The crystalline structure of InP/ZnS also remained unchanged after ligand exchange and Re-catalyst attachment. In addition, the main diffraction peak of InP/ZnS-2.3 nm exhibits a slight shift to the higher angle compared with InP/ZnS-3.3 nm and InP/ZnS-3.8 nm, which could be due to the pronounced lattice compression by the shell in smaller QDs. The absorption band edge and photoluminescence peak of the QDs shift to the longer wavelength with increasing sizes as shown in Figure 1a,b, respectively, which is consistent with a previous study.[20,21] Interestingly, the absorption spectra of QD/molecule complexes system show clear blue shift of the band edge and a diminishing of exciton band compared with their corresponding pristine quantum dots (Figure S3, Supporting

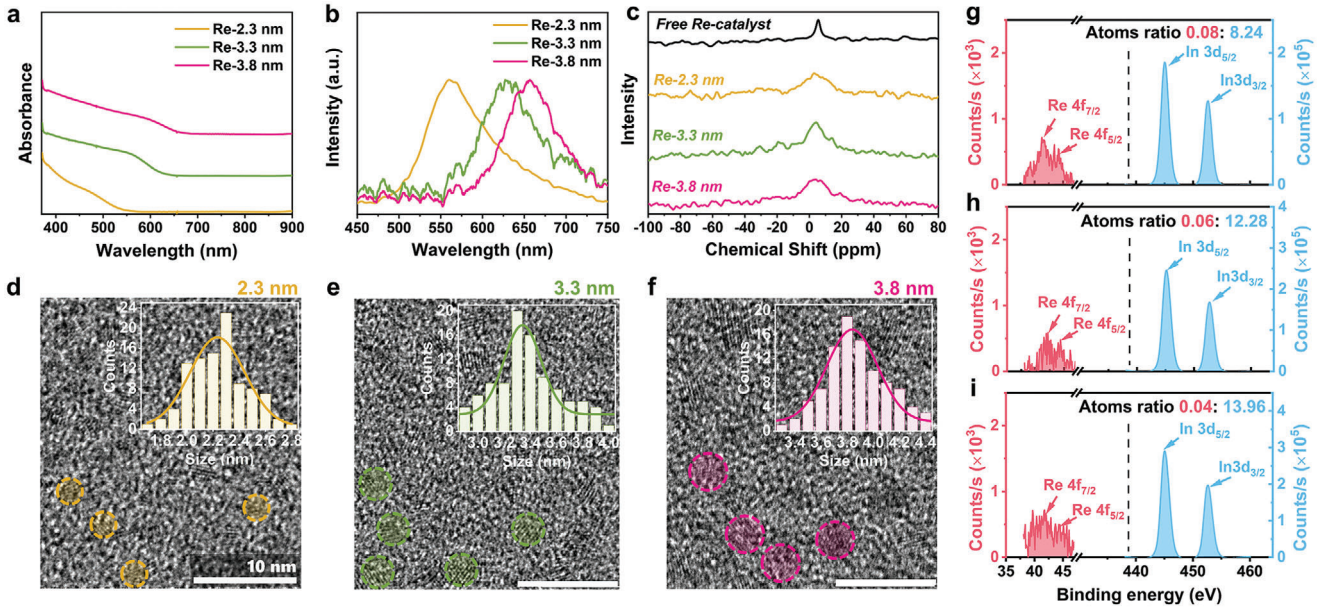

Figure 1. Structural characterization of the samples. UV–vis spectra a), photoluminescence spectra b), and ^{31}P NMR spectra c) of Re-2.3 nm, Re-3.3 nm and Re-3.8 nm. TEM characterization and size distribution histograms (inserts) for Re-2.3 nm d), Re-3.3 nm e) and Re-3.8 nm f), respectively. XPS spectra for the quantification of Re-catalyst concentration in Re-2.3 nm g), Re-3.3 nm h) and Re-3.8 nm i).

Information). This indicates dissociation of the charges from exciton and modification of the QDs electronic states via molecule attachment.

Fourier transform infrared (FT-IR) spectra for three QD/molecule systems presented two additional peaks arising at 2021 and 1900 cm^{-1}, as shown in Figure S4 (Supporting Information) corresponding to the intense C≡O stretching bonds of Re-catalyst,[24] which indicates the Re-catalyst is indeed tethered to QDs. In order to reveal the coordination mode between Re-complexes and QDs, phosphorus-31 nuclear magnetic resonance (^{31}P NMR) spectroscopy was first employed to identify the bonding type between QDs and Re-catalyst. As shown in Figure 1c, the significant broadening P peak at 5.5 ppm in the phosphate group for Re-2.3 nm, Re-3.3 nm, and Re-3.8 nm compared with pristine Re-catalyst illustrated that a substantial electron transfer process occurred between QDs and Re-catalyst. This confirmed that the Re-catalyst is covalently linked to the InP/ZnS quantum dot.[22] Note that the P signal for P element in InP/ZnS QD in ^{31}P NMR spectrum located in entirely different regions ≈−178 ppm.[23]

The amount of Re-photocatalysts attached to per InP/ZnS QD was quantified by X-ray photoelectron spectroscopy (XPS) measurement and calculated via precise atomic ratio between Re and In atoms since In atoms and Re atoms are the main elements and only exist in quantum dots and catalysts, respectively. Figure 1 shows Re 4f (42.18 and 44.28 eV) and In 3d (452.58 and 444.98 eV) core level emission spectra of Re-2.3 nm (Figure 1g), Re-3.3 nm (Figure 1h) and Re-3.8 nm (Figure 1i), respectively. The atomic ratios between Re and In are calculated to be 0.08: 8.24, 0.06: 12.28, and 0.04: 13.96, leading to approximately two Re-catalysts attached to per QD (**Table** 1). Inductively coupled plasma mass spectroscopy (ICP-MS) was also measured for all three samples, as summarized in Table S1 (Supporting Information). The molar mass of the core elements also confirmed the amount of the Re catalysts to the QDs. On the one hand, we proved that the multiple catalysts attached to one QD lead to enhanced CO_2-CH_4 production activity, as shown in Figure S5 (Supporting Information). On the other hand, we made a comparison of the excited state dynamics between QDs with one catalyst attachment and two catalysts attachment using transient absorption characterization. The TA kinetics at the maximum bleach, as shown in Figure S6 (Supporting Information), indicate that the electrons at the initial band edge excited state depopulate much faster (i.e., with faster decay at early time scale) in QDs with two catalyst attachments than one catalyst attachment when more than one electron-hole pairs are excited at one QD,

Table 1. Summary of calculation results for three samples.

Sample name	Size (diameter)	Unit cell in one QD	Ratio of In atom	Ratio of Re atom	The number of In atoms in one QD	The number of catalysts linked to one QD
Re-2.3 nm	2.3 nm	32	8.24	0.11	128	1.70
Re-3.3 nm	3.3 nm	94	12.28	0.06	376	1.83
Re-3.8 nm	3.8 nm	143	13.96	0.04	572	1.64

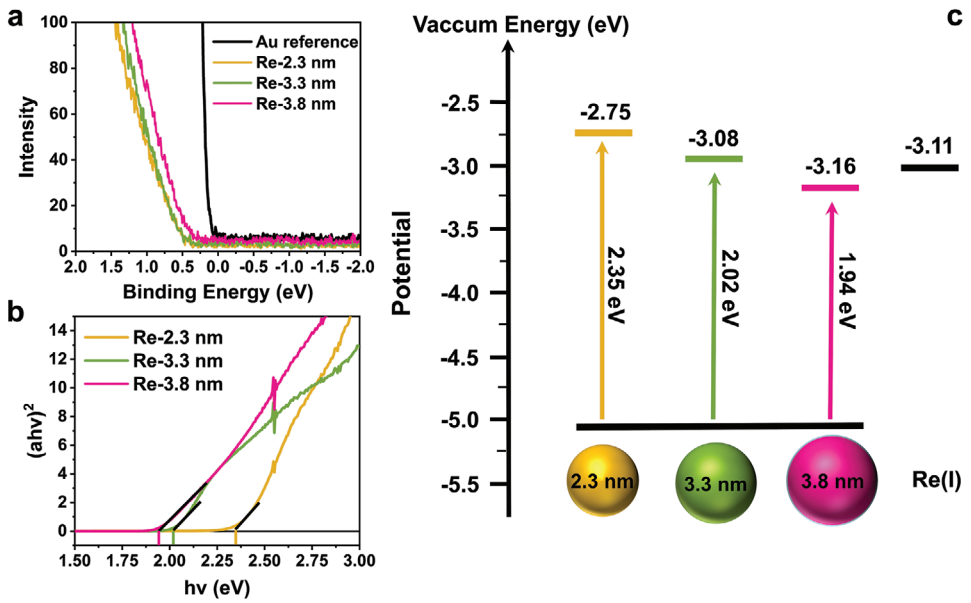

Figure 2. Determination of the band alignment in each sample. UPS spectra of each sample and gold reference a) and Tauc plot of absorption spectra b). Schematic of the Energy level, for illustrating the relative energy difference between each sample and Re-catalyst c).

indicating their fast electron transfer and efficient electron accumulation capability. This indicated multiple catalysts attached to one QD are expected to facilitate the multiexciton accumulation and donation. In this case, the electron injection could be performed in parallel instead of sequential mode. Therefore, in this work, we ensured two Re-catalyst attachments for all the targeted samples.

In order to reveal the QD size dependence on the charge transfer process, we first investigated the excited state structure of the specific hybrid system. We calculated the excited state structure of Re-QDs through TD-DFT calculation (for details, see supporting information). We observed that covalently coupled Re-Bpy exhibit strong frontier orbitals hybridization with QDs, The LUMO orbitals of the hybrid system already reside on the bipyridine moiety of the Re-catalyst, while the HOMO orbitals are dominantly contributed by the QDs (Figure S7, Supporting Information). Therefore, compared with pristine QDs where the excited exciton is localized in the QDs volume, excited electrons in Re-QDs undergo delocalization extending to the Bpy fragment. In this regard, efficient hybridization between frontier orbitals of Re-Bpy catalyst and QDs conduction band reduces the energy level of excited state and facilitate the exciton delocalization process, which leads to the slight blue shift and diminish of exciton band on absorption spectra compared with pristine QDs (Figure S3, Supporting Information). Furthermore, the significant quenching of pristine InP/ZnS QDs was observed clearly on the photoluminescence spectra (Figure S8, Supporting Information) after ligand exchange and was further quenched after Re-catalyst linking, which indicated photo-induced electrons were trapped by the dangling bond produced by ligand exchange and the efficient electron transfer from QDs to Re-catalysts.

In general, the optical band gap of InP/ZnS QDs is size-tunable due to the change of quantum confinement. Here, we confirm the energy state of each sample by ultraviolet photoemission spectra (UPS) and steady-state absorption measurement. As shown in **Figure** 2a, the valence band (VB) edge of each sample is almost the same in UPS spectra, with a binding energy of 0.5 eV versus the Fermi level. We also obtained their work function as 5.6 eV with an 80 eV photon energy (Figure S9, Supporting Information). The absolute value of the valence band maximum (VBM) could then be calculated to be −5.1 eV versus the vacuum level. Afterward, the optical band gap (Eg) of each sample was determined from the Tauc plot of the absorption spectra to be 2.35, 2.02, and 1.94 eV for Re-2.3 nm, Re-3.3 nm, and Re-3.8 nm, respectively (Figure 2b). The conduction band minimum of each sample was then deducted by adding the Eg to VBM to be −2.75, −3.08, and −3.16 eV for Re-2.3 nm, Re-3.3 nm, and Re-3.8 nm, respectively. Since the excited electrons in QDs are expected to be injected to Re(I), we also placed the redox level of Re(I) in ReBpy characterized via electrochemical measurement in our previous paper[24] to be −3.11 eV. The final energy band alignment of each sample is displayed in Figure 2c. It is clear that the conduction band (CB) levels Re-2.3 nm and Re-3.3 nm are higher than the Re(I) level, enabling electron injection. In contrast, the excited electron in Re-3.8 nm may be difficult to transfer to Re(I) center since its energetic unfavorable.

2.2. Excited State Dynamics

To rationalize the detailed mechanism of the photocatalytic reactions for Re-QDs hybrid system, excited state dynamics of each sample were studied by transient absorption (TA) spectroscopy with 470 nm excitation wavelength in order to avoid the direct excitation of Re-Bpy catalyst (for the absorption spectrum of Re-Bpy, see Figure S10, Supporting Information). Since CO_2 photoreduction is typically mediated by multi-electron donation, a comparison of excited state dynamics under single exciton and multiple

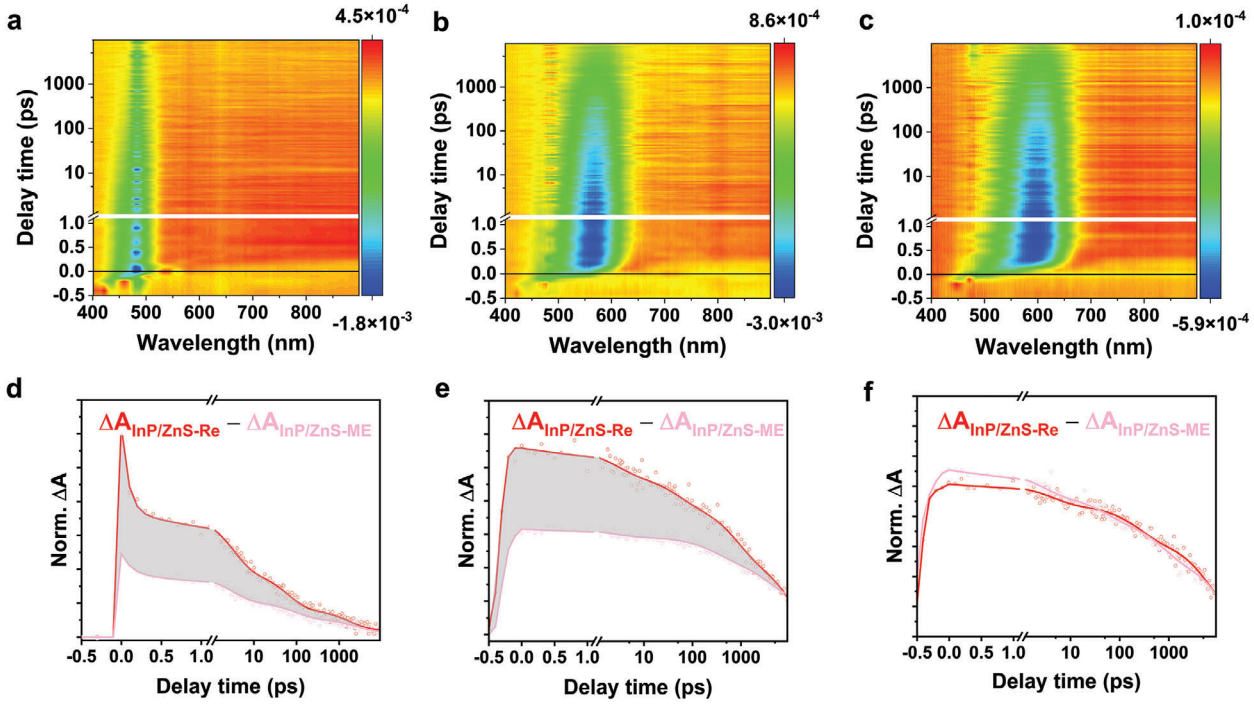

Figure 3. TA spectra and kinetics. 2D TA spectra of Re-2.3 nm a), Re-3.3 nm b) and Re-3.8 nm c) with 470 nm excitation wavelength. Extraction of TA kinetics for pure QD-Re catalysts for Re-2.3 nm d), Re-3.3 nm e) and Re-3.8 nm f). TA kinetics extracted from the minimum GSB, 457 nm for Re-2.3 nm, 570 nm for Re-3.3 nm, and 605 nm for Re-3.8 nm.

excitons population per QD after excitation is necessary to rationalize the catalytic performance. In this scenario, we selected two excitation intensities for the pump pulse to control the excitation density in each QD <N> (average number of excitons per QDs) ensuring only one electron or two electrons can be generated per excitation pulse for photocatalytic reactions (For details in excitation density calculation, see experimental section). **Figure 3**a–c exhibits typical 2D TA spectra of Re-QDs of different sizes with <N> = 0.50. All of the spectra feature a broad negative band at different positions corresponding to their absorption band edge, as shown in Figure 1a, which can be attributed to band-edge ground state bleach (GSB). Positive excited state absorption (ESA) in the red regions can also be observed. Those features indicate a rapid population of the band edge lowest excited state after excitation. The excited state dynamics was then studied by analyzing the kinetics of the GSB minimum which represents the depopulation dynamics of the lowest excited state. Before the study, it is indispensable to purify the TA kinetics of each sample since unattached QDs with Re-catalyst remain in the pool of QDs. As depicted in Figure 3d–f, this is achieved via subtracting kinetics of Re-QDs by that of InP/ZnS-ME (i.e., QDs without catalyst attachment) after normalizing the amplitude at long time decay (after 2 ns). We assume that the excited state of Re-QDs was depopulated entirely after such a long time decay due to the fast charge transfer process, the long-lived remaining GSB should be only contributed by residual QDs without Re-catalyst attachment.

The resulting differential TA kinetics of three samples after the subtraction process are shown in **Figure 4**a. GSB decay of Re-2.3 nm is much faster than that of Re-3.3 nm indicating the fast electron transfer process from initial excited state compared with Re-3.3 nm at early time scale <1 ps. In contrast, no differential kinetics of Re-3.8 nm can be observed after subtraction owing to identical GSB decay Re-3.8 nm and pristine QDs (Figure 3f), which suggested excited state depopulation pathway has been not changed after ReBpy attachment in this sample. For Re-2.3 nm QDs, TA kinetics can be fitted by three exponential decay components with lifetimes of 0.3 ps (21%), 8.0 ps (52%) and 367 ps (27%) as shown in **Table 2**. The assignment of these components can be achieved from the complementary analysis between TA and time-resolved IR spectroscopy measurements (TRIR) of the same sample. In time-resolved IR spectra of QD-Re samples (Figure S11, Supporting Information), we can observe broad featureless positive absorption as the fingerprint of free carriers after excitation, which is absent in neat QD samples and neat Re catalysts. This is because the electron-hole pairs in neat QDs are bounded within the exciton, while electrons in the Re-catalyst are also localized. Therefore, this signal can be assigned as dissociated free holes remaining in the QDs after electrons have been transferred to Re-centers. After comparing the kinetics of GB in TA and positive absorption in TRIR (Figure S12, Supporting Information), we can conclude that the subpicosecond component (0.3 ps) can be assigned to electron transfer from QDs to Re(I) center. It results from the dissociation of the excited exciton and generation of free holes in QDs that can be fingerprinted in TRIR in our previous study.[24] In addition, we confirmed via TD-DFT calculation that in our QD-Re system the LUMO level is dominantly contributed by the Bpy orbital, indicating the excited electrons already reside at Bpy moiety (for details see supporting information). Therefore, such a component refers to the fast electron injection from Bpy directly to Re(I) center. The 8.0 ps

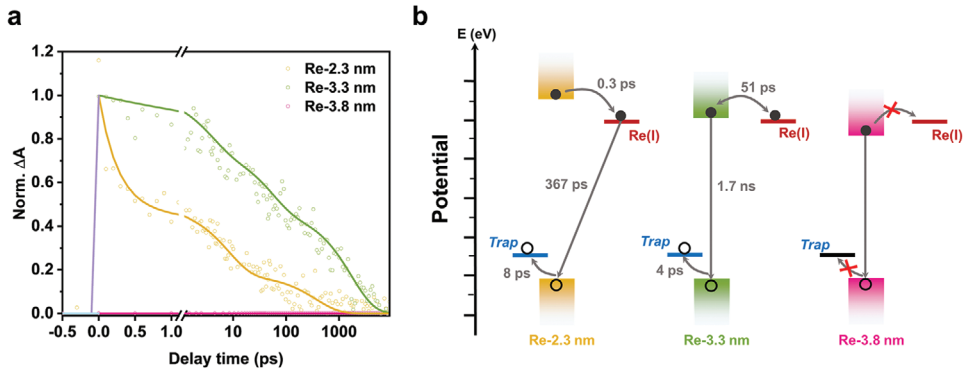

Figure 4. Single electron donation analysis. TA kinetics extracted from minimum GSB for all samples a) and corresponding excited state schematic diagram of lifetime and electron transfer pathway b). TA kinetics extracted from the minimum GSB, 457 nm for Re-2.3 nm, 570 nm for Re-3.3 nm, 605 nm for Re-3.8 nm.

component can be attributed to hole trapping by trap state produced by thiol ligand, which is commonly observed in thiol-capped QDs system with similar trapping time.[25] Finally, the 367 ps component should be correlated to the recombination Re center between the transferred electrons in Re(I) and residual holes in QDs (the recombination takes place in the QD). (For details of the analysis, see supporting information)

In contrast, the excited state depopulation in Re-3.3 nm is much slower as shown in Figure 4a. We can fit the TA kinetics of Re-3.3 nm by three exponential components as shown in Table 2. The lifetime of the fastest component (4 ps) is similar to the hole trapping process in Re-2.3 nm mentioned above. More importantly, the amplitude ratios of this component is also identical in two samples (i.e., 55% for Re-3.3 nm and 52% for Re-2.3 nm). This indicates it should also be attributed to a similar surface hole-trapping process. The longest component of 1.7 ns for Re-3.3 nm is close to the intrinsic exciton recombination time in InP QDs,[26] i.e., depopulation of the excited electrons on the CB of the QDs to the ground state. The middle component (51 ps) may correspond to the slow charge transfer to Re(I) due to the low driving force of the charge transfer comparable to the thermal energy k_BT (26 meV) as shown in Figure 4b.

We can rationalize the very different excited state dynamics in the three samples by their energy band alignment between the band edge states and energy level of Re(I) center as displayed in Figure 4b. The large driving force of electron transfer (i.e., $\Delta G = E_{cb}\text{-}E_{Re(I)} = 0.36$ eV) and short transfer distance[27] (i.e., distance between Bpy and Re(I) to be 0.208 nm)[28] guarantee the efficient electron transfer rate for Re-2.3 nm. In contrast, the driving force is only 0.03 eV for Re-3.3 nm, which is comparable to the thermal energy k_BT (26 meV). This means that the excited electrons will most probably hop back and forth between QDs and Re(I) center, and finally depopulate to the ground state from CB of QDs. Reversely, CB of Re-3.8 nm is lower than Re(I) meaning electron injection is suppressed. Similarly, no hole trapping is available, which may be because larger QDs have fewer surface traps during the Re attachment, and the driving force for hole traps (i.e., the energy difference between VBM and trap states) in large QDs is low.

Multi-electron donation plays a crucial role in photocatalytic CO_2 reduction. Subsequently we studied the photo-induced charge transfer dynamics of three samples with <N> > 1 to monitor whether multiple electrons excited in QDs can be efficiently injected to the multiple Re(I) at each QD for the CO_2 reduction. We implement the same subtraction operation as for the single electron donation analysis to remove the contribution from pristine QDs, and the result is shown in **Figure 5a**. All the kinetics can also be fitted by the multiexponential decay function. The fitted component of Re-2.3 nm is similar to single electron excitation condition (i.e., subpicosecond electron injection, picosecond hole trapping, as 100 ps electron-hole recombination) as shown in Table 2. This indicates that efficient electron transfers are kept the same when multiple electrons are excited in QDs since two catalysts have been attached per QDs ensuring a parallel charge transfer channel for each electron. However, the excited depopulation process for Re-3.3 nm in this case is much slower as shown in Figure 5a. In that sample, we found that the lifetime of the ps decay component remains the same, indicating the same hole-trapping process in Re-3.3 nm QD. The longest component of 2.7 ns can also be attributed to the single electron-hole recombination time identical to the single excitation case. The middle component with lifetime of 70 ps refers to Auger recombination of multiple exciton instead of multi-electron injection to Re(I) since the kinetics decay exhibit second order recombination feature (For details see supporting information). This means no efficient multi-electron transfer to Re(I) can be achieved for Re-3.3 nm sample. As clarified above, low driving force (0.03 eV) limits the electron transfer process. Secondly, subsequent electrons require overcome stronger Coulombic force from the first hole in QDs even if the first electron completes its transfer.[29]

Table 2. Multiexponential Fitting Parameters of TA for Re-QDs.

	<N>	A_1	t_1 [ps]	A_2	t_2 [ps]	A_3	t_3 [ps]
Re-2.3 nm	0.5	0.21	0.2 ± 0.1	0.52	8.0 ± 1.4	0.27	367 ± 85
Re-3.3 nm	0.5	0.55	51 ± 23	0.18	4.0 ± 1.8	0.23	1724 ± 262
Re-3.8 nm	0.5	0	0 ± 0	0	0 ± 0	0	0 ± 0
Re-2.3 nm	1.8	0.50	0.1 ± 0.01	0.31	3.0 ± 0.4	0.19	101 ± 15
Re-3.3 nm	1.8	0.25	8.0 ± 6.0	0.23	70 ± 63	0.52	2700 ± 508
Re-3.8 nm	1.8	0.22	100 ± 157	0.70	1100 ± 687	0.08	>>10000

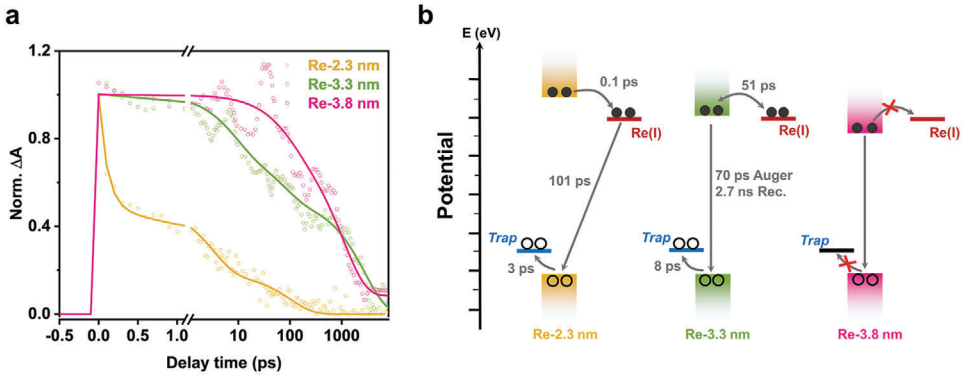

Figure 5. Multi-electron donation analysis. TA kinetics extracted from minimum GSB for all samples a) and corresponding excited state schematic diagram of lifetime and electron transfer pathway b). TA kinetics are extracted from the minimum GSB, 457 nm for Re-2.3 nm, 570 nm for Re-3.3 nm, 605 nm for Re-3.8 nm.

Considering the Re-3.8 nm QD, we start to see differentials signal different from single electron excitation scenario since the Auger process may be different between QDs and Re-QDs due to different dielectric screening effect of the surface ligand.[30–32] Therefore, the obtained 100 ps decay component should be attributed to the Auger recombination of multi-exciton in Re-3.8 nm, while 1.1 ns component is close to intrinsic single exciton lifetime in pristine QDs. Note the surface hole trapping process is still absent in Re-3.8 nm sample in this case. The overall charge transfer pathway and the corresponding lifetime are summarized in Figure 5b.

We finally investigated photocatalytic CO_2 reduction performance of the three Re-QDs. All the Re-QD samples were dispersed into CH_3CN and 10% triethanolamine (TEOA) as a sacrificial donor. To guarantee that only QDs were excited, the mixture was irradiated by an LED lamp with 440 excitation wavelength for 6 h after purging with Argon for 10 min. As shown in **Figure 6**a, Re-2.3 nm exhibits excellent photocatalytic performance of CO photoreduction with the turnover number (TON) of 52, corresponding to the overall apparent quantum yield (AQY) of 7%, which is much higher than 11 (AQY of 0.73%) for Re-3.8 nm and 9 (AQY of 0.82%) for Re-3.3 nm, and respectively. It should first be noted that the signal in Figure 6a,b only comes from the CO_2 photoreduction, not from the decomposition of samples or sacrificial agent, according to the ^{13}C isotope labeling experiment shown in Figure S14 (Supporting Information).

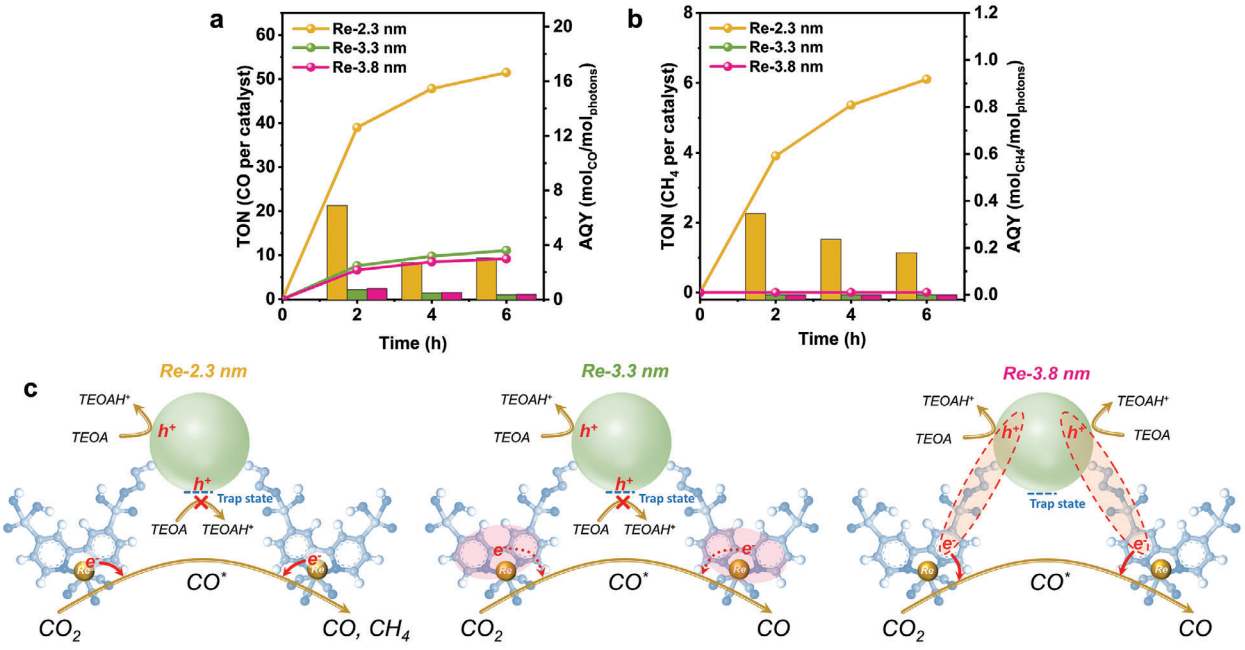

Figure 6. Photocatalytic reduction CO_2 performance. Photocatalytic evolution (curves) of CO a) and CH_4 b) and corresponding AQY (bars) for three samples. Schematic illustration of pathways for photocatalytic reduction of CO_2 with two Re-catalyst attachment c). Light pink region in Re-3.3 shows the electron transfer reversely to Re(I) center, and the dotted line refers to the electrons that not likely to participate in the photocatalytic reduction of CO_2 reactions.

According to the above discussion, both single-electron donation and multi-electron donation are efficient in Re 3.3 nm, facilitating CO_2 reduction. Note that even though the surface hole trapping occurred in Re-2.3 nm, there still remains 50% QDs in the QD pool free from the hole trapping where the excited holes can be scavenged by the electron donated from sacrificial agent TEOA. In contrast, both Re-3.3 nm and Re-3.8 nm suffered from inefficient electron transfer to Re(I). In this scenario, the excited electron residing in the Bpy moiety of Re-catalyst according to the DFT calculation can still participate in CO_2 reduction in the media but with much less efficiency than the transferred electron at Re(I) due to 1) a much shorter lifetime, and 2) longer distance between electrons at Bpy and the absorbent CO_2 species. As a result, the CO production yield is much less. We also noticed that Re-3.3 nm exhibits slightly higher CO production activity than Re-3.8 nm. Such subtle deviation could be originated from many factors. Our above analysis indicates that Re-3.3 nm is more prone to charge transfer to the Re-center after excitation than Re-3.8 nm due to the high band edge excited state. On the other hand, smaller QDs may generate more surface traps restricting charge separation and donation, which might compensate for the difference in the electron transfer dynamic. Besides that, other factors like differences in the capability of surface adsorption due to different surface areas could also influence the final catalytic performance.

More importantly, an efficient multi-electron donation in Re-2.3 nm facilitated 8-electron mediated photocatalytic production of CH_4 as shown in Figure 6b with a TON of 6 after 6 h reaction, corresponding to the overall AQY of ≈0.9%. Such values are among the highest within all the state-of-the-art inorganic and organic photocatalysts for CO_2 photo-catalytic methanation.[33,34] As illustrated in Figure 6c, excited QD in Re-2.3 nm undergoes effective exciton delocalization due to unconventional electronic structure, photoinduced holes accepted electrons from TEOA which promoted charge separation. Eventually, a fast electron transfer process occurs simultaneously on two catalysts as depicted in Figure 6c, efficient multi-electron donation enables photocatalytic CH_4 evolution. On the other hand, Re-3.3 nm and Re-3.8 nm QDs have excited electrons either localized between Re(I) center and Bpy or entirely bonded within initial excitons, preventing the electron donation for the CO_2 reduction, explaining their inferior CO and absent CH_4 production. Moreover, photocatalytic performance was also conducted in control samples such as pristine InP/ZnS QDs and InP/ZnS-ME with the size of 2.3 nm (Figure S15, Supporting Information), which suggested efficient photo-conversion of CO_2 to CO and CH_4 can only be achieved by QD/molecule complex system with optimal band alignment for efficient multi-electron donation process.

3. Conclusion

In summary, we prepared three InP/ZnS colloidal quantum dots with different sizes and successfully attached two Re-catalysts onto each QDs via covalent bonding. The characterization on their electronic structure revealed that the energy alignment between CB of the QDs and LUMO level of Re-catalysts is strongly QD size dependent, where the CB level of Re-2.3 nm QDs is higher than the ReBpy level, while 3.3 and 3.8 nm QDs have CB level close and lower than the Re level, respectively. As a result, Re-2.3 nm exhibits excellent electron injection from QDs to Re-catalyst. Such injection is valid for both single excitation and multiple excitation modes for each QDs due to the two Re-catalysts attachment. In contrast, Re-3.3 nm and Re-3.8 nm QDs showed inefficient electron transfer processes due to insufficient driving force. Therefore, only Re-2.3 nm exhibited CO_2 reduction efficiency where both two-electron mediated product CO and 8-electron mediated product CH_4 can be obtained with TON to be 52 and 6 corresponding to overall AQY of 7% and 1%, respectively. This work can be considered as guidance for future material engineering on photocatalysts for CO_2 photocatalytic reduction with optimal efficiency and selectivity. Based on the conclusion of this paper, we can draw a relative universal design suggestion for the QD-catalyst to promote multi-electron donation for efficient CO_2 reduction: 1) In order to provide highly reduced products, the driving force required for the electron transfer to the reduction level is larger than the low reducted products. This is due to the internal Coulombic attribution force that hinders the multiple electron donation. This can be solved by either increasing the surface reaction centers or lifting the LUMO level of the catalyst. 2) Trade-off factors remain regarding the size of QDs to be selected in QD-catalyst, where the electronic band structure and surface trap density obviously play opposite roles in catalytic activity. Therefore, there should always be an optimal medium QD size for the CO_2 photocatalytic reaction. This work demonstrates the critical effect of QDs size on the electronic band alignment in QD-catalyst hybrid structures and consequently dominates the efficiency of multi-electron donation for catalytic CO_2 reduction.

4. Experimental Section

Materials for Synthesis: The photocatalyst ($Re(bpy)(CO)_3Br$) was prepared according to previous literature procedures.[35] Indium(III) chloride (98%, Sigma–Aldrich), zinc(II) chloride (98%, Sigma–Aldrich), zinc(II) iodide (98%, Sigma–Aldrich), oleylamine (technical grade, 70%, Sigma–Aldrich), tris(diethylamino)phosphine (98%, Sigma–Aldrich), sulfur powder (99.98%, Sigma–Aldrich), trioctylphosphine (TOP, 97%, Sigma–Aldrich), 2-mercaptoethanol (ME, 99%, Sigma–Aldrich), chloroform (99.5%, Sigma–Aldrich), ethanol (EtOH, for HPLC, VWR Chemicals), hexane (HEX, for HPLC, VWR Chemicals), dimethylformamide (DMF, for HPLC, VWR Chemicals), and toluene (for HPLC, VWR Chemicals).

Synthesis of InP/ZnS QDs with the Size of 2.3 nm: The process of synthesis InP/ZnS quantum dot was prepared by previous literature[20] with a little modification. Briefly, the mixture of 111 mg (0.5 mmol) of indium(III) chloride as indium precursor, 320 mg (1.0 mmol) zinc(II) iodide, and 136 mg (1.0 mmol) of zinc(II) chloride as zinc precursor was dissolved into 5 mL (15 mmol) of oleylamine, then evacuated by Schlenk techniques and kept under vacuum at 120 °C for 1 h. Afterward, the reaction system was heated to 180 °C under an Argon atmosphere. 0.5 mL (1.8 mmol) of tris(diethylamino)phosphine (phosphorous:indium ratio = 3.6:1) was quickly injected into the mixture. The system was kept at 180 °C for 30 min to drive the growth of InP quantum dot to completion and was further heated to 260 °C and slowly added 1 mL of TOP-S (2 м) solution at the rate of 0.2 mL mi^{-1}n. TOP-S solution was prepared by dissolving 0.128 g of sulfur powder in 2 mL of TOP under an inert atmosphere. The system was kept at 260 °C for 3 h to passivate the InP QDs. Finally, the system was cooled down to room temperature. To purify InP/ZnS QDs, ≈10 mL of EtOH was added for the precipitation of QDs. After centrifugation, the supernatant was discarded and the precipitated QDs were further dissolved into HEX subsequent centrifugation. Then the precipitation was discarded, keep the supernatant and precipitation in

15 mL of EtOH. Following centrifugation, the QDs were again dispersed into 20 mL HEX and centrifuged to remove the insoluble impurities. The prepared QDs were kept well in solution at 2–6 °C.

Synthesis of InP/ZnS QDs with the Different Sizes: Size of InP/ZnS QDs was modulated by the different concentration ratio of zinc(II) iodide and zinc(II) chloride precursers and the InP core growth temperature. The main process of synthesis is decribed above. In summary, when 306 mg (2.25 mmol) of zinc(II) chloride was added, 3.3 nm of InP/ZnS was obtained; when added 306 mg (2.25 mmol) of zinc(II) chloride and the temperature of InP core growth increased to 260 °C from 180 °C, 3.8 nm of InP/ZnS was obtained.

Synthesis of InP/ZnS-ME QDs: InP/ZnS-ME was prepared by ligand exchange method according to the previous literature[36] with slight modification. Briefly, most of the solvent (HEX) in the as-prepared InP/ZnS QDs solution was first removed by the rotary evaporation approach. Then ≈2500 times molar excess of ME was added to the reaction system. The mixture was heated to 90 °C under a vacuum to remove the rest of HEX. Afterward, the reaction mixture was kept at 90 °C under Argon atmosphere for ≈1 h or less until the solution became clear. After cooling down to room temperature, chloroform was added to precipitate the resulting ME-decorated InP/ZnS QDs (ME-capped QDs, InP/ZnS-ME). Centrifugation at 5000 rpm for ≈5 min yielded the targeted products and easily dispersed into DMF. The prepared InP/ZnS-ME were kept well in solution at 2–6 °C.

Synthesis of Re-2.3 nm, Re-3.3 nm, and Re-3.8 nm: The mixture of 1: 2 molar mass ratio of InP/ZnS-ME and $Re(bpy)(CO)_3Br$ was evacuated and injected argon gas by Schlenk techniques three times, then the system was heated to 110 °C under argon atmosphere for 3 h. Following cooling down to room temperature, toluene was added for precipitation of Re-QDs, and centrifugation at 5000 rpm for ≈5 min was used to purify the products. Finally, the precipitation was easily dispersed into DMF, and kept the solution at 2–6 °C in dark place for further measurement.

Photocatalytic Reduction of CO_2: The method of photocatalytic reduction of CO_2 was carried out according to literature methods with a little modification. 5 mL of CH_3CN, and 0.5 mL of TEOA (triethanolamine) contained with ≈2 µM of Re-QDs were put in 10 mL septum-sealed glass vials. The mixture was purged with Ar for 10 min and CO_2 for 15 min to wipe out air, and then irradiated by a LED lamp with 440 wavelengths (light intensity: 83.8 mW cm^{-2}; irradiation area: 0.25 cm^2) for 6 h and kept stirring during the photocatalytic reaction. The amount of CO and CH_4 generated was quantified every 1 h by using Shimadzu gas chromatography (GC-2010) by analyzing 500 µL of the headspace. The control experiment was also carried out only in the absence of CO_2.

Powder X-Ray Diffraction (XRD): X-ray diffraction (PXRD) data were collected by using Rigaku Miniflex600 at room temperature with Cu Kα1 source (λ = 1.5418 Å) over the range of $2\theta = 3.0 - 90.0°$ with a step size of 0.02° and a counting time of 1 s per 10 step.

TD-DFT Computational methods: To investigate the relationship of the optical properties with molecular structures and electronic structures, Re-QDs (Tables S1 and S2, Supporting Information) were constructed to represent one quantum dot connected with one and two Re-catalytic centers. An implicit solvent model was used to reflect the solvation environment and implemented using SMD solvation model[37] in Gaussian 16 package.[38] PBE0[39–41] was selected as the exchange-correlation functional; def2-SVP[42,43] was selected as the basis set for DFT calculations. Acetonitrile parameters were used to represent the solvents in the SMD models.[44] Time-dependent density functional theory (TD-DFT) calculations were also performed using these parameters.

Fourier-Transformed Infrared Spectroscopy: Fourier-Transformed Infrared Spectroscopy (FT-IR) data were obtained by using ALPHA P FT-IR spectrometer (Bruker). The sample materials were prepared to KBr pellet.

X-ray Photoelectron Spectroscopy: X-ray Photoelectron Spectroscopy (XPS) data were got by using XPS-Thermo Scientific with Al Kα (1486 eV) as the excitation X-ray source. The pressure of the analysis chamber was maintained at 2×10^{-10} mbar during measurement. The sample material was prepared by dispersing it in DMF and then dripping it onto a silicon wafer then dried in air. The peak of C 1s at ≈284.8 eV was used to calibrate the energy scale. The XPS data were performed to precisely quantify the number of Re-catalyst tether to one quantum dot by integrating the area of atom peaks. The absorption spectra were measured in a UV–vis absorption spectrophotometer from Agilent Technologies (Santa Clara, USA).

Photoluminescence: Photoluminescence (PL) was performed via Spex Fluorolog 1681 standard spectrofluorometer.

Transmission Electron Microscopy: Transmission electron microscopy (TEM) images were obtained with a Tecnai G2 T20 TEM.

Nuclear Magnetic Resonance (NMR) Measurement: All presented NMR spectra were either measured on a Bruker Avance IIIHD spectrometer operating at a ^{31}P frequency of 242.93 MHz (14.1 T) equipped with a 5 mm Bruker BBFO probe, or a Bruker Avance III Nanobay operating at a ^{31}P frequency of 161.97 MHz (9.4 T) equipped with a 5 mm CryoProdigy probe. For the quantum dots with attached photo catalyst 65–75k scans were accumulated with an interscan delay of 1.5 s, 30° flip-angle and ^1H power-gated decoupling. For the free photo catalyst 16 scans were accumulated with an interscan delay of 2.5 s, 90° flip-angle and ^1H power-gated decoupling. The samples were measured "as-prepared" adding only 5 vol.% of DMF-d^7 for lock and shimming. Chemical shifts are reported relative to H_3PO_4 using the lock signal from DMF-d^7.

Transient Absorption (TA) Spectroscopy Measurements: The transient absorption (TA) measurements were carried out by laser-base pump-probe spectroscopy with the laser power intensity equating to less than one phonon and two phonons absorption per quantum dot. Laser pulse (800 nm, 40 fs pulse length, 2 KHz repetition rate) were generated by a femtosecond oscillator (Mai Tai SP, both Spectra Physics). Excitation pulse at the wavelength of 470 nm to ensure the pulse only exciting the light harvester (quantum dots) not photocatalyst, which generated an optical parametric amplifier (Topas C, Light Conversion). For the probe, a broad supercontinuum spectrum was generated from a thin sapphire crystal and split by a beam splitter into a probe pulse and a reference pulse. The probe pulse and the reference pulse were dispersed in a spectrograph and detected by a diode array (Pascher Instruments). A Berek compensator in the pump beam was placed to set the mutual polarization between pump and probe beams to magic angle (54.7°). Excitation power intensity and spot size were necessary for the calculation of excitation fluence, and further determined the average number of excitons $\langle N \rangle$ per QDs.

Transient Mid-IR Absorption Spectroscopy: A frequency-doubled Q-switched Nd:YAG laser (Quanta-Ray ProSeries, Spectra-Physics) was employed to obtain 450 nm pump light, 10 mJ $pulse^{-1}$ with a FWHM of 10 ns. The 450 nm pump light was used through the MOPO crystal to pump the sample. Probing was done with the continuous wave quantum cascade (QC) IR laser with a tuning capability between 1893 and 2300 cm^{-1} (Daylight Solutions). For IR detection, a liquid nitrogen-cooled mercury cadmium-telluride (MCT) detector (KMPV10–1J2, Kolmar Technologies, Inc.) was used. The IR probe light was overlapped with the pump beam in a quasi-co-linear arrangement at 25° angle. Transient absorption traces were acquired with a Tektronix TDS 3052 500 MHz (5 GS/s) oscilloscope in connection with the L900 software (Edinburgh Instruments) and processed using Origin 2021 software. Samples were kept in a modified Omni cell (Specac) with O-ring sealed CaF2 windows and a path length of 1 mm. All samples were re-prepared to keep fresh before measurement, and DMF was used as a solvent in all experiments.

Ultraviolet Photoelectron Spectroscopy (UPS): The UPS measurements were carried out using the PEEM endstation of the MAXPEEM beamline at MAX IV laboratory in Lund, Sweden. the micro-spot XPS mode of the PEEM instrument was utilized to measure the local XPS from a spot with a size of 5 µm on the sample. This enabled for this study to mount multiple samples on a single substrate and measure them simultaneously. During sample preparation, dispersion drops containing quantum dots in four different sizes were deposited on a single Au-plated Si wafer using a pipette. After drying in a desiccator, the drops turned into coffee-ring shapes with an average diameter of 1 mm. These drops were spaced apart from each other to facilitate independent measurements on each of them, as well as on the bare Au area between the samples. This method allowed all UPS measurements from different samples to be automatically aligned on the energy scale, without the need for further calibration, as all the samples were electrically connected through the Au substrate. The substrate with samples was loaded into the PEEM chamber and measured under ultra-high vacuum (UHV) conditions with a base pressure better

than 1×10^{-10} torr. To ensure that the UPS data collected from the samples did not contain contributions from the Au substrate, thick areas were selected where no Au 4f signals could be detected. The energy resolution of the instrument in this operation mode is ≈100 meV, and the photon energy used in the measurement was 80 eV.

Absorption Cross Section Determination: High excitation fluence could excite QDs to multiple exciton states. With a usual assumption, the initially generated multiple exciton population follows the Poissonian distribution

$$P_N = \frac{e^{-\langle N\rangle} \cdot \langle N\rangle^N}{N!} \tag{2}$$

where $\langle N\rangle$ is the average number of excitons per QDs, N is the number of excitons and P_N is the fraction of NCs with N excitons. $\langle N\rangle = \sigma \bullet I$ could be used to present the average number of excitons per NCs, where σ is the absorption cross-section at the excitation wavelength and I is the excitation intensity in units of the number of photons per pulse per excitation area. From Equation (1), the fraction of excited NCs, P_{exc}, as could be calculate:

$$P_{exc} = \sum_{N=1}^{\infty} P_N = 1 - P_0 = 1 - e^{-\langle N\rangle} = 1 - e^{-\sigma \cdot I} \tag{3}$$

If P_{exc} was known, σ could be calculated from (2). P_{exc} was optained by measuring the excitation intensity dependence of the late-time region signal ($t \geq 1$ ns), which corresponds to the last remaining exciton after the Auger process. Due to multiple excitations generated at high pump intensity excitation in NCs is rapidly lost via Auger process leaving only one excitation at late-time region ($t \geq 1$ ns). The signal $\Delta A_0(I, t \geq 1\ ns)$ intensity could be rescaled to the corresponding signal at t = 0, which could be called as $\Delta A_0(I)$. the lowest excitation intensity was used as reference excitation intensity and corresponding average number of excitons per NCs, $\langle N\rangle_0$.as reference number of excitons per QDs.

$$\Delta A_0\ (I) = \frac{\Delta A0\ (I,\ t \geq 1\ ns)}{e^{-\frac{t}{\tau}}} = \Delta A_0 \cdot \left(1 - e^{-\left(I \cdot I_0 \cdot \langle N\rangle_0\right)}\right) \tag{4}$$

ΔA_0, denotes the largest possible single-exciton signal rescaled to t = 0.

Based on the rescaled signal $\Delta A_0(I)$, an exponential fit was performed to Equation (4). From the fitting, the value of $\langle N\rangle_0$ was gotten, and absorption cross-section σ of InP/ZnS QDs at 400 nm (3.1 eV) was calculated. The absorption cross-section σ at 450 nm was calculated based on the values of σ at 400 nm and absorption spectra. The calculated result is shown in Figure S13 (Supporting Information).

Calculation Details of the Apparent Quantum Yield (AQY): The energy of one photon (E_{photon}) with the wavelength of λ_{inc} (nm) is calculated by the following equation:

$$E_{photon} = \frac{hc}{\lambda_{inc}} \tag{5}$$

where h (J·s) is Planck's constant, c ($m \cdot s^{-1}$) is the speed of light and λ_{inc} (m) is the wavelength of the incident monochromatic light.

The total energy of the incident monochromatic light (E_{total}) is calculated by the following equation:

$$E_{total} = I_{inc}\ St \tag{6}$$

where I_{inc} ($W \cdot m^{-2}$) is the power density of the incident monochromatic light, S (m^2) is the irradiation area and t (s) is the the duration of the incident light exposure.

According to the Beer–Lambert law:

$$A = \frac{I_{inc}}{I_{tra}} = \varepsilon cL \tag{7}$$

Where A is the measured absorbance, I_{inc} ($W \cdot m^{-2}$) is the intensity of the incident light at a given wavelength, I_{tra} ($W \cdot m^{-2}$) is the transmitted intensity, L (m) the path length through the sample, and c ($mol \cdot L^{-1}$) the concentration of the absorbing species.

Then the power density of absorbed monochromatic light (I_a) by catalysts is:

$$I_a = I_{inc} - I_{tra} \tag{8}$$

Then the power density of absorbed monochromatic light (I_a) by catalysts is:

$$E_a = E_{total} - E_{tra} = (I_{inc} - I_{tra})St \tag{9}$$

The number of absorbed photons (N_{photon}) by catalysts could be obtained through the following equation:

$$N_{photon} = \frac{E_a}{E_{photon}} = \frac{(I_{inc} - I_{tra})St\lambda_{inc}}{hc} \tag{10}$$

The moles of incident photons (n_{photon}) absorbed by catalysts could be obtained through the following equation:

$$n_{photon} = \frac{N_{photon}}{N_A} = \frac{(I_{inc} - I_{tra})St\lambda_{inc}}{hcN_A} \tag{11}$$

Where N_A (mol^{-1}) is the Avogadro constant.

Finally, The AQY is calculated by the number of molecules Nmol undergoing an event (conversion of reactants or formation of products) relative to the number of photon N_{ph} absorbed by the photocatalyst in the following expression:

$$\varphi_{AQY} = \frac{n_{mol}\left(mol\ s^{-1}\right)}{n_{ph}\left(einstein\ \ s^{-1}\right)} \tag{12}$$

InP/ZnS QDs, InP/ZnS-ME and Re-QDs Concentration Calculation: All samples including InP/ZnS QDs, InP/ZnS-ME, and Re-QDs could be considered as InP-based quantum dots. InP-based quantum dots concentration was determined by Beer–Lambert law

$$A = \varepsilon cl \tag{13}$$

where A is the absorption of the sample, ε is the molar extinction coefficient, c is the concentration of InP based quantum dots, l is the optic path length in cm. If ε was known, c could be calculated from (12). ε could be obtained by the empirical formula reported by previous literature:[45]

$$\varepsilon_{410} = (1.29 \pm 0.06) \times 10^4 d_{QD}^3 \tag{14}$$

where ε_{410} is the molar extinction coefficient of samples at 410 nm excitation wavelength, d_{QD} is the size of InP based quantum dots confirmed by TEM. It should be note that A is the absorption of samples at 410 nm.

Determination of the Number of Re-Catalyst Attaching to Per InP/ZnS Quantum Dot: For InP based quantum dots, their lattice parameter value a is 0.5861 nm and 4 indium atoms in complete unit cell, which reported by previous literature.[46] The Volume of InP/ZnS is calculated by equation followed:

$$V = \frac{4}{3}\pi d_{QD}^3 \tag{15}$$

where d_{QD} is the size of InP based quantum dots. The number of unit cell of InP for per InP/ZnS QD is easy to obtain to be 32 and 128 indium atoms for per InP/ZnS QD. Then the number of In and Re atom in sample could be calculated by the ratio of indium and rhenium in XPS spectra, the numbers of Re-catalyst were confimred via the number of Re atom as only

one Re atom was located per Re-catalyst. The calculated results of three samples in this work is followed: (Table 1).

Supporting Information

Supporting Information is available from the Wiley Online Library or from the author.

Acknowledgements

Q.Z, M.A, and Y.C contributed to this work equally. This work is supported through a research grant (VIL50350) from VILLUM FONDEN, Denmark, the Swedish Research Council (No. 2021–05319), and the National Natural Science Foundation of China (22209135). Q.Z. acknowledge the financial support from the Chinese Scholarship Council. J.M. acknowledges the financial support from VILLUM FONDEN (58626), the Carl Trygger Foundation and the Royal Physio-graphic Society of Lund.

Conflict of Interest

The authors declare no conflict of interest.

Date Availability Statement

The data that support the findings of this study are available from the corresponding author upon reasonable request.

Keywords

methane, multi-electron donation, photocatalytic reduction of CO_2, quantum dot, size-dependent

Received: December 10, 2023
Revised: February 23, 2024
Published online:

[1] S. N. Habisreutinger, L. Schmidt-Mende, J. K. Stolarczyk, *Angew. Chem., Int. Ed.* **2013**, *52*, 7372.
[2] T. Banerjee, K. Gottschling, G. Savasci, C. Ochsenfeld, B. V. Lotsch, *ACS Energy Lett.* **2018**, *3*, 400.
[3] P. Akhter, M. A. Farkhondehfal, S. Hernández, M. Hussain, A. Fina, G. Saracco, A. U. Khan, N. Russo, *J. Environ. Chem. Eng.* **2016**, *4*, 3934.
[4] H. Kumagai, Y. Tamaki, O. Ishitani, *Acc. Chem. Res.* **2022**, *55*, 978.
[5] P. Gotico, T. T. Tran, A. Baron, B. Vauzeilles, C. Lefumeux, M. H. Ha-Thi, T. Pino, Z. Halime, A. Quaranta, W. Leibl, A. Aukauloo, *ChemPhotoChem* **2021**, *5*, 654.
[6] X. Yi, J. Zhao, W. Wu, D. Huang, S. Ji, J. Sun, *Dalton Trans.* **2012**, *41*, 8931.
[7] J. Fu, K. Jiang, X. Qiu, J. Yu, M. Liu, *Mater. Today* **2020**, *32*, 222.
[8] E. Vol'pin, I. S. Kolomnikov, Coordination Chemistry-XIV **1973**, 567.
[9] Z. W. Yang, J. M. Chen, L. Q. Qiu, W. J. Xie, L. N. He, *Angew. Chem., Int. Ed. Engl.* **2022**, *61*, 202205301.
[10] Y. Yamazaki, T. Onoda, J. Ishikawa, S. Furukawa, C. Tanaka, T. Utsugi, T. Tsubomura, *Front. Chem.* **2019**, *7*, 288.
[11] J. Huang, M. G. Gatty, B. Xu, P. B. Pati, A. S. Etman, L. Tian, J. Sun, L. Hammarström, H. Tian, *Dalton Trans.* **2018**, *47*, 10775.
[12] B. Chon, S. Choi, Y. Seo, H. S. Lee, C. H. Kim, H. J. Son, S. O. Kang, *ACS Sustainable Chem. Eng.* **2022**, *10*, 6033.
[13] J. Huang, B. Xu, L. Tian, P. B. Pati, A. S. Etman, J. Sun, L. Hammarström, H. Tian, *Chem. Commun.* **2019**, *55*, 7918.
[14] Z. C. Kong, H. H. Zhang, J. F. Liao, Y. J. Dong, Y. Jiang, H. Y. Chen, D. Bin Kuang, *Sol. RRL* **2020**, *4*, 1900365.
[15] T. Morimoto, C. Nishiura, M. Tanaka, J. Rohacova, Y. Nakagawa, Y. Funada, K. Koike, Y. Yamamoto, S. Shishido, T. Kojima, T. Saeki, T. Ozeki, O. Ishitani, *J. Am. Chem. Soc.* **2013**, *135*, 13266.
[16] T. Asatani, Y. Nakagawa, Y. Funada, S. Sawa, H. Takeda, T. Morimoto, K. Koike, O. Ishitani, *Inorg. Chem.* **2014**, *53*, 7170.
[17] J. Y. Xu, X. Tong, P. Yu, G. E. Wenya, T. McGrath, M. J. Fong, J. Wu, Z. M. Wang, *Adv. Sci.* **2018**, *5*, 1800221.
[18] C. Liu, F. Qiu, J. J. Peterson, T. D. Krauss, *J. Phys. Chem. B* **2015**, *119*, 7349.
[19] X. Xiang, J. Fielden, W. Rodríguez-Córdoba, Z. Huang, N. Zhang, Z. Luo, D. G. Musaev, T. Lian, C. L. Hill, *J. Phys. Chem. C* **2013**, *117*, 918.
[20] S. Yu, X. B. Fan, X. Wang, J. Li, Q. Zhang, A. Xia, S. Wei, L. Z. Wu, Y. Zhou, G. R. Patzke, *Nat. Commun.* **2018**, *9*, 9.
[21] J. Meng, Q. Zhao, W. Lin, T. Pullerits, K. Zheng, *Adv. Electron. Mater.* **2023**, *9*, 2300369.
[22] Z. Hens, I. Moreels, J. C. Martins, *ChemPhysChem* **2005**, *6*, 2578.
[23] M. Tomaselli, J. L. Yarger, M. Bruchez, R. H. Havlin, D. De Graw, A. Pines, A. P. Alivisatos, *J. Chem. Phys.* **1999**, *110*, 8861.
[24] Q. Pan, M. Abdellah, Y. Cao, W. Lin, Y. Liu, J. Meng, Q. Zhou, Q. Zhao, X. Yan, Z. Li, H. Cui, H. Cao, W. Fang, D. A. Tanner, M. Abdel-Hafiez, Y. Zhou, T. Pullerits, S. E. Canton, H. Xu, K. Zheng, *Nat. Commun.* **2022**, *13*, 13.
[25] K. Zheng, K. Žídek, M. Abdellah, W. Zhang, P. Chábera, N. Lenngren, A. Yartsev, T. Pullerits, *J. Phys. Chem. C* **2014**, *118*, 18462.
[26] B. Zhang, X. Wang, D. Wang, J. Tang, X. Fang, D. Fang, X. Wang, R. Chen, T. He, Z. Wei, *J. Phys. Chem. C* **2019**, *123*, 27207.
[27] E. E. Benson, K. A. Grice, J. M. Smieja, C. P. Kubiak, *Polyhedron* **2013**, *58*, 229.
[28] E. E. Benson, C. P. Kubiak, *Chem. Commun.* **2012**, *48*, 7374.
[29] K. Žídek, K. Zheng, M. Abdellah, N. Lenngren, P. Chábera, T. Pullerits, *Nano Lett.* **2012**, *12*, 6393.
[30] A. Haug, W. Ekardt, *Solid State Commun.* **1975**, *17*, 267.
[31] X. Hou, J. Kang, H. Qin, X. Chen, J. Ma, J. Zhou, L. Chen, L. Wang, L. W. Wang, X. Peng, *Nat. Commun.* **2019**, 10.
[32] X. Hou, H. Qin, X. Peng, *Nano Lett.* **2021**, *21*, 3871.
[33] Q. Li, S. Wang, Z. Sun, Q. Tang, Y. Liu, L. Wang, H. Wang, Z. Wu, *Nano Res.* **2019**, *12*, 2749.
[34] Y. Lu, M. Liu, N. Zheng, X. He, R. Hu, R. Wang, Q. Zhou, Z. Hu, *Nano Res.* **2022**, *15*, 3042.
[35] C. D. Windle, E. Pastor, A. Reynal, A. C. Whitwood, Y. Vaynzof, J. R. Durrant, R. N. Perutz, E. Reisner, *Chem. - Eur. J.* **2015**, *21*, 3746.
[36] M. Li, M. B. Zaman, D. Bardelang, X. Wu, D. Wang, J. C. Margeson, D. M. Leek, J. A. Ripmeester, C. I. Ratcliffe, Q. Lin, B. Yang, K. Yu, *Chem. Commun.* **2009**, *44*, 6807.
[37] A. V. Marenich, C. J. Cramer, D. G. Truhlar, *J. Phys. Chem. B* **2009**, *113*, 6378.
[38] M. Caricato, A. Frisch, J. Hiscocks, M. J. Frisch, *Gaussian 09 IOps Reference*, 2nd Ed., Gaussian, Inc., Wallingford, USA **2003**.
[39] J. P. Perdew, K. Burke, M. Ernzerhof, *Phys. Rev. Lett.* **1996**, *77*, 3865.
[40] C. Adamo, V. Barone, *J. Chem. Phys.* **1999**, *110*, 6158.
[41] M. Ernzerhof, G. E. Scuseria, *J. Chem. Phys.* **1999**, *110*, 5029.
[42] F. Weigend, R. Ahlrichs, *Phys. Chem. Chem. Phys.* **2005**, *7*, 3297.
[43] F. Weigend, *Phys. Chem. Chem. Phys.* **2006**, *8*, 1057.
[44] O. Borodin, W. Behl, T. R. Jow, *J. Phys. Chem. C* **2013**, *117*, 8661.
[45] J. Ministro, MSc Thesis, University of Ghent, Gent, Belgium **2013**.
[46] W. Hui, L. Sherin, S. Javed, S. Khalid, W. Asghar, S. A. Fufa, *Complexity* **2022**, *2022*, 9707749.